Available online at www.sciencedirect.com
ScienceDirect
Trans. Nonferrous Met. Soc. China 33(2023) 2076−2089
Transactions of Nonferrous Metals Society of China
www.tnmsc.cn

Influence of heterogeneous microstructures on anodization behavior and biocompatibility of Ti−15Zr alloy

Han-chun TANG[1], Da-peng ZHAO[2], Chang-jun WAN[2],
Xiao-song LI[2], Xiao-wei JI[2], Jin-cheng TANG[3], Yuan-kui CAO[1], Yong LIU[1]

1. State Key Laboratory of Powder Metallurgy, Central South University, Changsha 410083, China;
2. College of Biology, Hunan University, Changsha 410082, China;
3. Department of Materials Science and Engineering,
Southern University of Science and Technology, Shenzhen 518055, China

Received 7 March 2022; accepted 14 September 2022

Abstract: The influence of heterogeneous microstructures on the anodization behavior and biocompatibility of Ti-based alloys was investigated. A heterogeneous Ti−15Zr alloy was fabricated by powder metallurgy, followed by hot rolling and heat treatments. Electrochemical anodization was then applied to obtaining a nanotube-arrayed surface. The results show that the surface of the anodized heterogeneous Ti−15Zr alloy consists of nano-sized tube structure as well as micron-scaled tubular clusters and microcracks. The formation of such a surface should be attributed to the (0001)-oriented striped grains and the heterogeneous Zr distribution. Compared with the anodized arc-melted Ti−15Zr control group, the anodized heterogeneous Ti−15Zr exhibits comparable super-hydrophilicity, better protein adsorption, and improved cell proliferation, mainly due to the hierarchical surface structures of the latter.

Key words: Ti−Zr alloy; electrochemical anodization; compositional heterogeneity; preferred orientation; biocompatibility

1 Introduction

Nowadays, titanium (Ti) and its alloys are the most popular dental implant materials, due to their high specific strength, good corrosion resistance, and superior biocompatibility [1]. Commercially pure titanium (CP-Ti) and Ti−6Al−4V are still the most widely used biomedical titanium-based materials. However, the low strength, wear resistance, and corrosion resistance of the former, and the potentially toxic elements Al and V in the latter significantly limit their potential for long-term biomedical applications [2]. Zr is a non-toxic and non-allergenic element, so Ti−Zr alloys usually show excellent biocompatibility [3]. Besides, previous studies also have revealed that the addition of Zr into Ti can improve the mechanical properties [4] and corrosion resistance [5]. So, Ti−Zr alloys have attracted extensive attention for dental applications [6].

Surface characteristics, including chemical composition and surface topography, can significantly influence the success of implant treatment [7]. Therefore, various surface technologies have been applied to Ti-based implants, and have progressed from bioinert Ti-based surfaces to bioactive ones. For instance, micro-/nano-scaled structures usually show better biocompatibility compared to polished surfaces [8]. The great specific surface area of the well-controlled hierarchical surface can not only improve

Corresponding author: Da-peng ZHAO, Tel: +86-731-88822606, E-mail: dpzhao@hnu.edu.cn
DOI: 10.1016/S1003-6326(23)66245-4
1003-6326/© 2023 The Nonferrous Metals Society of China. Published by Elsevier Ltd & Science Press

cell attachment, proliferation, and/or differentiation but also benefit integration with newly formed bone [9]. The micron- or sub-micron-scaled surface is more advantageous for cell adhesion [10,11], while nano-scaled microstructure often leads to osteoblast differentiation and tissue regeneration, especially the nanotubes prepared by electrochemical anodization (EA) [12].

The fabrication of titania (TiO_2) nanotube arrays is one of the most promising nano-engineering approaches for surface bioactivation and functionalization of Ti-based implants [13]. For example, the angiogenic behavior was significantly improved after introducing nanotubes with a diameter of 70 nm on Ti−6Al−4V [14]. Besides the commonly-used commercially pure Ti and Ti−6Al−4V, other Ti-based materials, such as Ti−Nb [15], Ti−Zr [16], and Ti−Nb−Ta−Zr alloys [17], were also used as the substrates for EA treatments. However, many studies show contradictory results about the influence of the microstructure of Ti-based substrates on the morphology and growth of nanotubes [18]. For instance, MACAK et al [19] claimed that grain boundaries should be responsible for the disturbed nanotube growth on CP-Ti. But in another work [20], no differences in nanotube geometry were observed on different Ti substrates varying in grain size.

At present, Ti−15Zr alloy has been successfully used in clinical dental applications, and no side effects were reported up to now [21]. Ti−15Zr implants (Roxolid®) have equally good survival and success rates compared to conventional Ti Grade IV implants for mandibular removable overdentures [22]. In our recent work, a strong-yet-ductile Ti−15Zr, showing heterogeneous microstructure, was successfully fabricated [23]. The Zr-rich and Zr-lean "dual-phase" microstructure provided a unique model to investigate the influence of the chemical and microstructural heterogeneity of the Ti−Zr matrix on nanotubes, and the anodization properties and biological response of the nanotube arrays on Ti−Zr alloys. In this work, a Ti−15Zr alloy with a "dual-phase" microstructure was prepared by powder metallurgy, followed by anodization to obtain a micro-/nano-scaled surface. The effects of microstructures on the formation of micro-/nano-scaled nanotube structures and the biocompatibility of the heterogeneous alloy were investigated.

2 Experimental

2.1 Material preparation

A Ti−15Zr (wt.%) alloy was prepared by blending elemental powders of Ti (purity >99.9%, particle size <45 μm) and Zr (purity >99.9%, particle size <75 μm), followed by cold isostatic pressing (CIP) at a pressure of 180 MPa. Afterward, the compacts were sintered at 1400 °C in a vacuum (10^{-3} Pa), followed by hot rolling at 750 °C. Then, the samples were reheated at 600 °C and water quenched. Besides, reference Ti−15Zr samples were fabricated by vacuum arc-melting. The ingots were melted at least eight times to ensure the homogeneity. The above-mentioned Ti−15Zr samples prepared via the powder-metallurgy process and arc-melting are referred to as PM and AM, respectively.

Both PM and AM samples were used as substrates for electrochemical anodization. The samples were ultrasonically cleaned, and then anodized for 50 min in a two-electrode electrochemical cell at a constant voltage of 30 V. The electrolyte containing 0.5 wt.% NH_4F was continuously agitated by a magnetic stirrer during anodization. After anodization, the samples were cleaned ultrasonically in ethylene glycol for 10 min, washed with deionized water, and dried. The electrochemical anodized PM and AM samples are termed PM-EA and AM-EA, respectively.

2.2 Surface characterization

X-ray diffraction (XRD) analyses were performed on a Rigaku D/max 2550VB+. X-ray diffractometer with Cu K_α radiation (40 kV, 300 mA, step size 0.02°). The XRD patterns were recorded in a 2θ range of 10°−80°. The grain size and microstructures of AM sample were characterized by using optical microscopy (OM, Leica MeF3A). Scanning electron microscope (SEM, FEI Quanta FEG 250) equipped with an energy dispersive spectroscopy (EDS) unit was used for surface characterization. The grain size of PM samples was evaluated by double-beam electron microscope (FEI Helios Nanolab G3) equipped with an electron back scattered diffraction (EBSD) probe. In the tapping mode of the atomic force microscope (AFM, MFP−3D Stand Alone), the roughness of the surfaces of AM-EA and PM-EA was characterized

by a probe. The regions with the size of 5 μm × 5 μm were randomly selected for both configurations. The acquired images were analyzed using Asylum Research software. The surface roughness parameters, i.e., R_a (arithmetical mean deviation of the profile), R_q (root mean square deviation of the profile), and R_z (maximum height of the profile), were measured according to the standard JIS B 0601: 2001 (ISO 4287—1997). An FEI Tecnai 20 transmission electron microscope (TEM) was applied for further characterization of the nanotubes on AM-EA and PM-EA. The fast Fourier transformation (FFT) patterns were obtained by high-angle resolution TEM images. The chemical composition analyses of nanotubes were performed by the TEM unit equipped with EDS. An X-ray photoelectron spectrometer (XPS, ESCALAB250Xi) was also employed for the composition analyses. The wettability of Milli-Q water on samples was evaluated by the contact angle analyzer (SDC−200S, Sindin, China), and at least three tests were repeated on each sample.

2.3 Protein adsorption assay

Bovine serum albumin (BSA), fraction V (Sigma, 99.8% in purity) was used as the model protein. BSA was diluted in phosphate-buffered saline (PBS, K_2HPO_4/KH_2PO_4, 100 mmol/L, pH 7.4) to a protein solution at a concentration of 1 mg/mL. The four sets of samples, i.e., PM, AM, PM-EA, and AM-EA, were put into a 24-well plate and incubated in the protein solution at 37 °C for 2 h. Next, the samples were washed 3 times with PBS, and then, transferred into a new 24-well plate. The proteins on the samples were eluted with 2% sodium dodecyl sulfate (SDS) for 1 h at 37 °C and then assayed by a protein assay kit (Pierce, BCA protein assay kit). Samples were analyzed using a microplate reader at 450 nm. The protein concentration was calibrated with bovine serum albumin by a standard curve. Four sets of samples were incubated in the same way in BSA protein and then stained with FITC for 12 h. Then, the samples were washed 3 times with methanol and once with PBS. Finally, the samples were observed with a laser confocal microscope (Olympus FV1200).

2.4 Cell culture

The four configurations, i.e., PM, AM, PM-EA, and AM-EA, were sterilized in a high-temperature sterilization pot at 120 °C for 100 min, and then dried in a vacuum drying oven for 30 min. After that, the up and down surfaces were irradiated under ultraviolet light for 10 min each.

Human osteosarcoma (MG63) cells supplied by China Infrastructure of Cell Line Sources were cultured in McCoy's 5A medium (Gibco, USA), 15% fetal bovine serum (FBS, Gibco, USA), and 1% penicillin/streptomycin (Gibco, USA), with an atmosphere of 5% CO_2 at 37 °C. The sterilized sample was washed twice with PBS, and then, put into the culture medium. MG63 cells were added to the culture medium and seeded at a density of 20000 cells per well. After culturing for 24 h, the cells were washed with PBS three times, fixed with 3.5% paraformaldehyde (PFA) for 0.5 h at 4 °C, and dehydrated by 20%, 40%, 60%, 80%, 95%, 100% ethanol for 10 min each.

2.5 Cell proliferation

MG63 cells were cultured for 5 d on samples. Cell counting kit-8 (CCK-8, Dojindo, Japan) solution at a content of 10% of the total was added to each well. The solutions were taken out on Day 3 and Day 5 and incubated at 37 °C for 1 h, and finally detected by a microplate reader (Perkin-Elmer, USA) at 450 nm.

2.6 Statistical analysis

All experiments were repeated at least three times. The data were shown as mean ± standard deviation. In order to compare the differences in protein concentration and cell proliferation among four groups, the one-way analysis of variance was performed using SPSS Statistics 20 software (IBM, USA). The homogeneity of variances was assessed with Levene's Test.

3 Results and discussion

3.1 Phase, microstructure, and chemical composition

Figure 1 presents the XRD patterns of AM, PM, AM-EA, and PM-EA. Since Zr is usually accepted as a neutral element in Ti alloy [24], it can be expected to present only the α-Ti phase in AM and PM. The absence of crystallized TiO_2 phase (e.g., anatase-type and rutile-type) in AM-EA and PM-EA samples indicates that the nanotubes in the two configurations are probably amorphous,

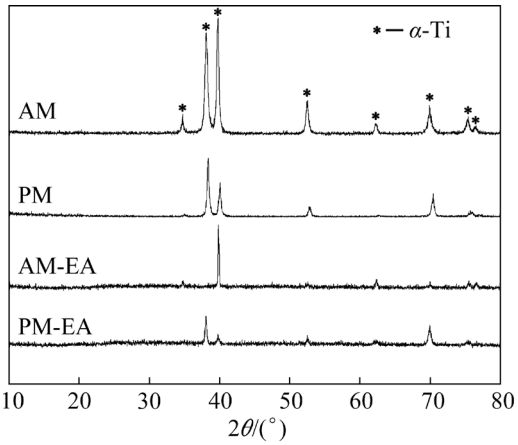

Fig. 1 XRD patterns of AM, PM, AM-EA and PM-EA

which is very common for the as-anodized Ti-based materials [13].

Figure 2(a) shows the OM image of AM. AM presents coarse equiaxed crystal grains with the grain size of about 1000 μm, which is typical for arc-melted Ti alloys. Figure 2(b) presents the SEM image of the surface parallel to the rolling plane of PM. The absence of visible pores in PM indicates that the samples are almost completely dense after hot rolling. Stretched structures lie along the rolling direction, and white stripes are shown among grey areas. The binarized image of Fig. 2(b) and the corresponding distance map are shown in Figs. 2(c, d). The dark regions (with a grey value of 0) and bright regions (with a grey value of 255) in Fig. 2(c) correspond to the grey areas and white stripes, respectively. As shown in Fig. 2(d), the average width of the white stripes is 675 nm.

EDS mapping images were performed in Fig. 3 to better understand the element distribution in the AM and PM samples. AM shows a fully homogeneous distribution of Ti and Zr, but the distribution of the two elements in PM exhibits a strong dependence on the areas. For example, the white stripes are Zr-enriched laths, while the grey areas are Ti-enriched. Table 1 gives the EDS results of Point *A* and Point *B* in Fig. 2(b), representing the Zr-enriched laths and the Ti-enriched regions, respectively. The Zr content in the Zr-enriched laths is almost three times higher than that in the Ti-enriched regions. The presence of such a strong heterogeneous composition distribution should be probably attributed to the spinodal decomposition of the α phase in the Ti−Zr system, especially in a deformed Widmanstätten-like structure [23,25].

Figure 4 shows the results of the EBSD analyses of the surface parallel to the rolling plane of PM. Figure 4(a) presents the inverse pole figure (IPF) and image quality (IQ) map along the rolling direction. The color in Fig. 4(a) offers a measure of the grain orientation normal to the EBSD plane, and

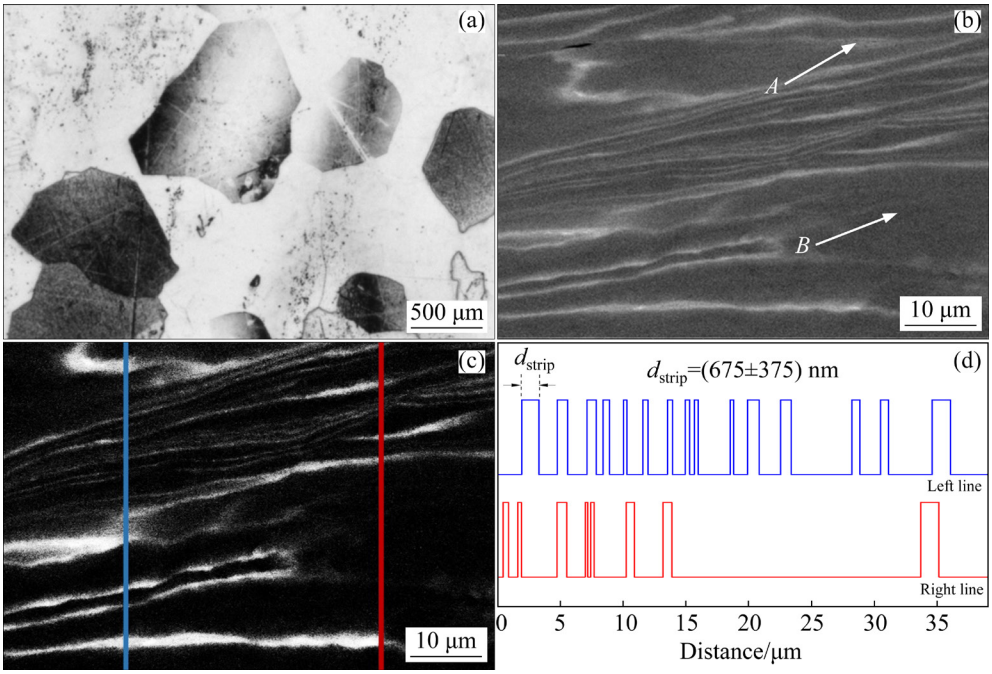

Fig. 2 Microstructures of AM and PM samples: (a) OM image of surface of AM; (b) SEM image of surface of PM parallel to rolling plane (Points *A* and *B* are in the white strip and grey area, respectively); (c) Binarized SEM image of Fig. 2(b); (d) Corresponding distance map of Fig. 2(c) (d_{strip} is the width of white strips)

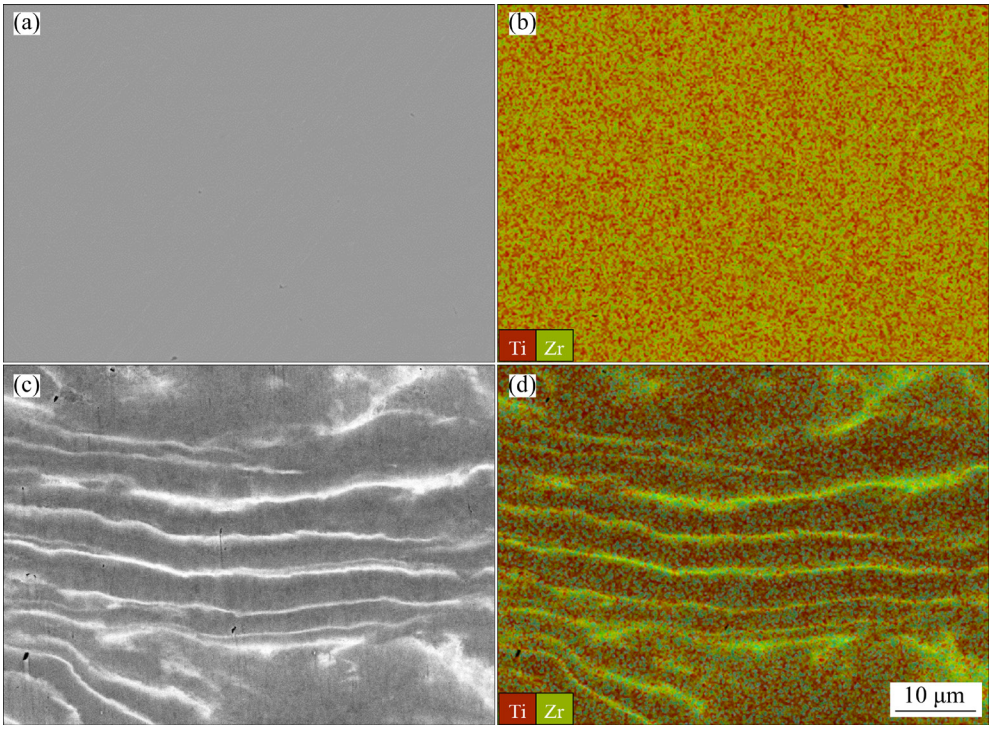

Fig. 3 Composition distributions of AM and PM samples: (a) SEM image of AM; (b) EDS mapping image of AM; (c) SEM image of PM; (d) EDS mapping image of PM

Table 1 EDS results of points in Fig. 2(b) (wt.%)

Point	Ti	Zr
A	79.7	20.3
B	92.5	7.5

each solid color corresponds to an individual grain. As one can see from the color palette in the upper right corner of Fig. 4(a), most grains in striped laths are red, while, and the grains in other regions are mainly green and blue. The significant difference in color between the laths and other areas suggests that Zr-enriched laths and Ti-enriched regions exhibit different preferred orientations of the grains (so-called texture). The grains in striped laths are mainly (0001) grains, i.e., the *c*-axis of the grains tends to be perpendicular to the plane of EBSD mapping. However, most grains in Ti-enriched regions present $(10\bar{1}0)$ and $(2\bar{1}\bar{1}0)$ preferred orientations. Besides, Fig. 4(a) also indicates the significantly different sizes of the grains in Zr-enriched laths and Ti-enriched regions. The area fraction data as shown in Fig. 4(b) clearly confirm the bimodal distribution of grain size of PM. The sizes of most grains are below 10 μm, while, only around 13% of grains are in the range from 15 to 20 μm.

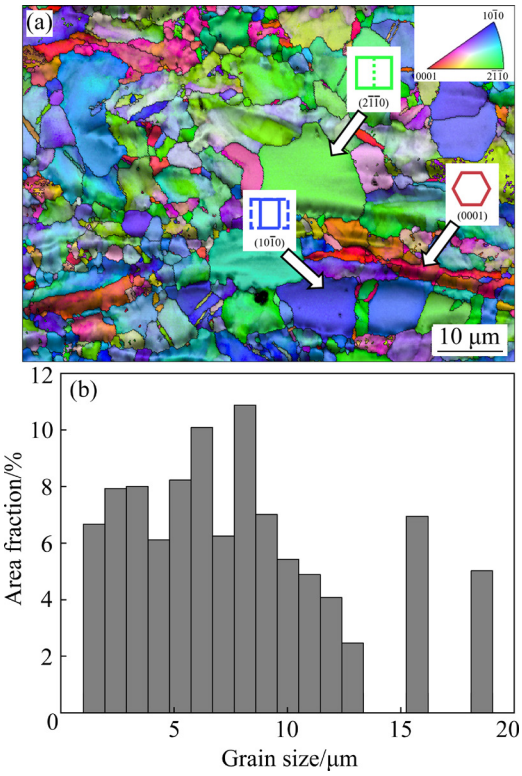

Fig. 4 IPF and IQ map of surface parallel to rolling plane of PM, showing color-coding of IPF map at upper right corner, and schematic oriented hexagonal unit cell placed beside corresponding grain with specific orientation (a); Grain size distribution of PM evaluated by EBSD (b)

Compared with the millimeter-scaled as-cast grains in AM as shown in Fig. 2(a), the grain sizes of PM are all much finer (all below 20 μm). Such a difference should be mainly attributed to the grain elongation, fragmentation, and dynamic recrystallization during hot rolling. Most $(10\bar{1}0)$-oriented blue grains and $(2\bar{1}\bar{1}0)$- oriented green ones as shown in Fig. 4(a) exhibit equiaxial morphology, indicating that the dynamic recrystallization is probably complete in Ti-enriched regions. However, the (0001)-oriented red grains usually show elongated structure, implying the incomplete recrystallization in Zr-enriched strips after hot rolling and the following heat treatment.

Figures 5(a, b) show the nanotube arrays on AM-EA. At low magnification (see Fig. 5(a)), the nanotubes disperse uniformly on the surface except for some minor voids, which is quite typical for anodized Ti alloys [8]. The high magnification SEM image as shown in Fig. 5(b) presents a relatively smooth nanotubular surface with a nanotubular diameter of (82.7±3.2) nm. KIM and CHOE [26] prepared arc-melted Ti−Zr alloys, showing similar flat nanotube surfaces as on AM-EA. KONATU et al [27] also anodized the arc-melted Ti−15Zr alloy, and obtained a very flat nanotube surface. After heat treatment at different temperatures, the nanotube surface remains flat. In contrast, the nanotube distribution on PM-EA seems to be quite heterogeneous as presented in Figs. 5(c, d). The nanotubes are distributed as clusters, leaving oriented microcracks between the adjacent clusters as marked by yellow arrows in Fig. 5(c). At high magnification (see Fig. 5(d)), the nanotubular diameters are measured as (81.2±8.6) nm, which is almost the same as those of nanotubes on AM-EA. It is important to note that many nanotubes at the

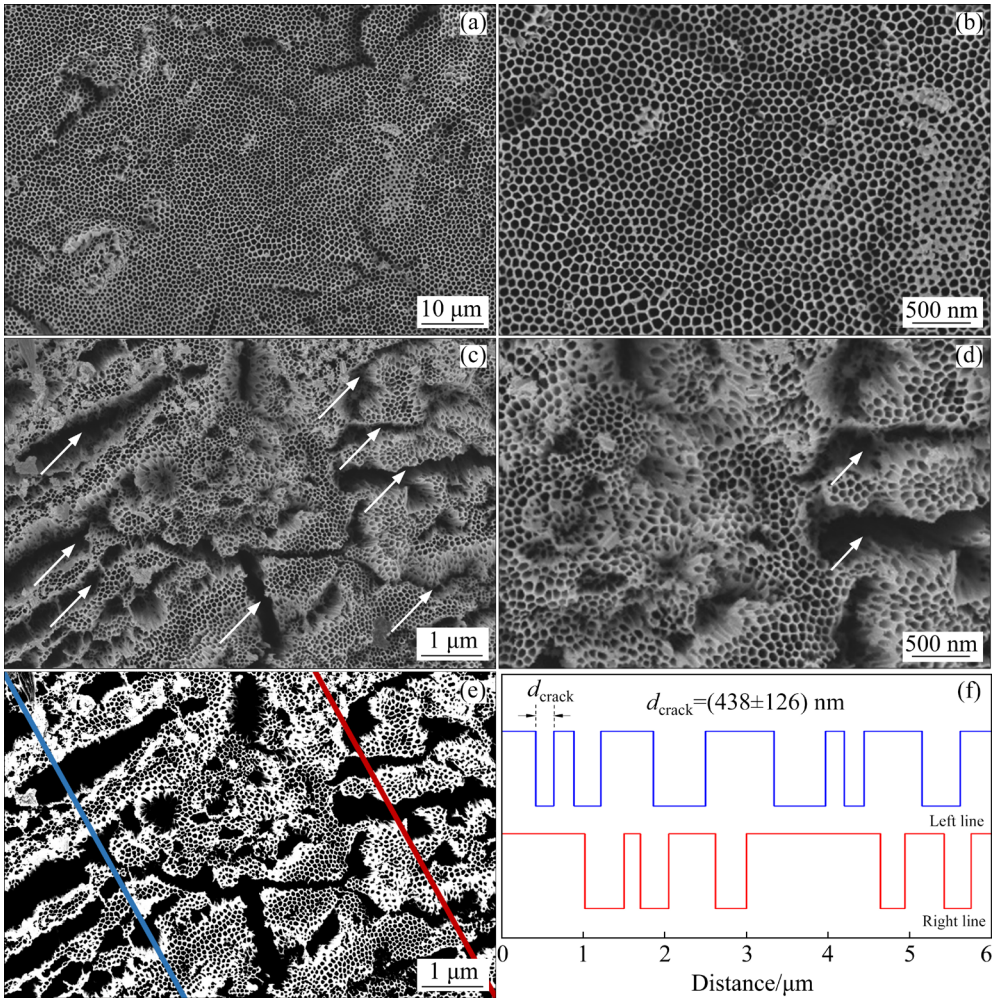

Fig. 5 SEM images of surface of AM-EA (a, b); SEM images of surface of PM-EA (the yellow arrows show the microcracks) (c, d); Binarized SEM image (e) of Fig. 5(c); Corresponding distance map of Fig. 5(e) (d_{crack} is the width of microcracks) (f)

outer layer of clusters tend to bend to the cluster center, and the heights of the nanotube clusters differ from each other. The binarized SEM image of nanotube arrays on PM-EA is shown in Fig. 5(e). The bright areas (with a grey scale of 255) and dark regions (with a grey scale of 0) correspond to the nanotube clusters and the oriented microcracks among them. It should be highlighted that although the average width of the microcracks as shown in Fig. 5(f) seems to be lower than that of the white strips as presented in Fig. 2(d), there is no statistically significant difference between d_{crack} and d_{strip}.

AFM was applied to evaluating the topographical features of AM-EA and PM-EA. The 3D images in the range of 5 μm × 5 μm provide a visual display of the surfaces of both samples as presented in Figs. 6(a, b). It seems that PM-EA exhibits higher and more irregular peak dimensions than AM-EA. Such diversity is further confirmed by the roughness values of R_a, R_q, and R_z, as given in Table 2. Compared with the profile of AM-EA, that of PM-EA presents much higher R_a, R_q, and R_z, indicating that the surface of the latter configuration shows enhanced surface profile deviation and greater surface area ratio (the ratio of the real surface area to its geometrical projection). Consequently, PM-EA shows a much rougher micron-scaled surface topography compared with AM-EA.

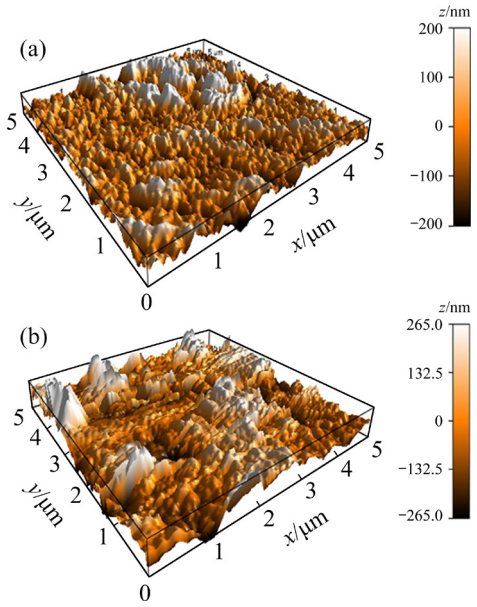

Fig. 6 3D views of surface of nanotubes: (a) AM-EA; (b) PM-EA

Table 2 Roughness values of AM-EA and PM-EA surfaces

Sample	R_a/nm	R_q/nm	R_z/nm
AM-EA	80.8	103.3	954.3
PM-EA	115.5	149.4	1704.7

Figures 7(a, b) show the cross-sectional SEM images of anodic oxide nanotubes formed on AM-EA and PM-EA samples. The nanotubes on both configurations exhibit similar lengths. The tube length of AM-EA is about 1.8 μm, and that of PM-EA is about 2.2 μm. The nanotubes can be closely combined with their matrix, since a compact oxide layer is usually formed between the nanotubes and the substrate [28].

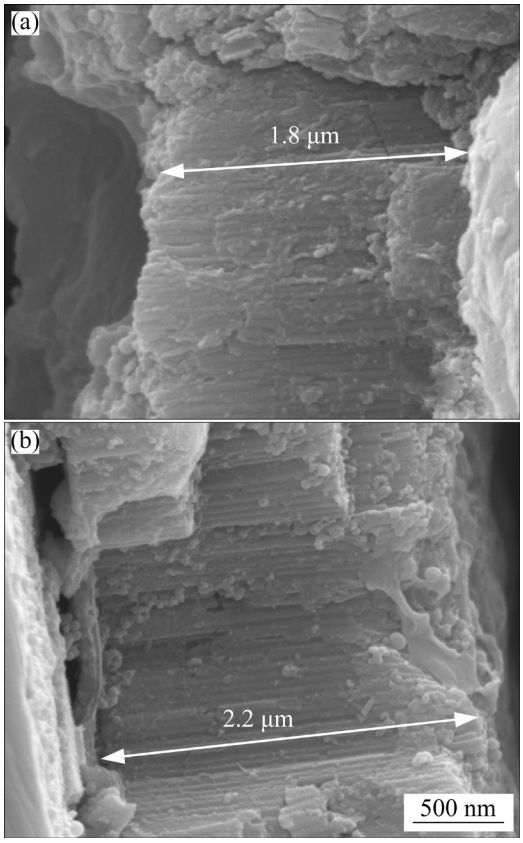

Fig. 7 Cross-sectional SEM images of anodic oxide nanotubes: (a) AM-EA; (b) PM-EA

Figures 8(a, b) show the cross-sectional TEM images of anodic oxide nanotubes formed on AM-EA and PM-EA samples. The nanotubes on both configurations exhibit similar lengths (i.e., ~1.2 μm). Figures 8(c, d) reveal the amorphous state of the nanotubes on AM-EA and PM-EA samples. It has been reported that the nanotubular

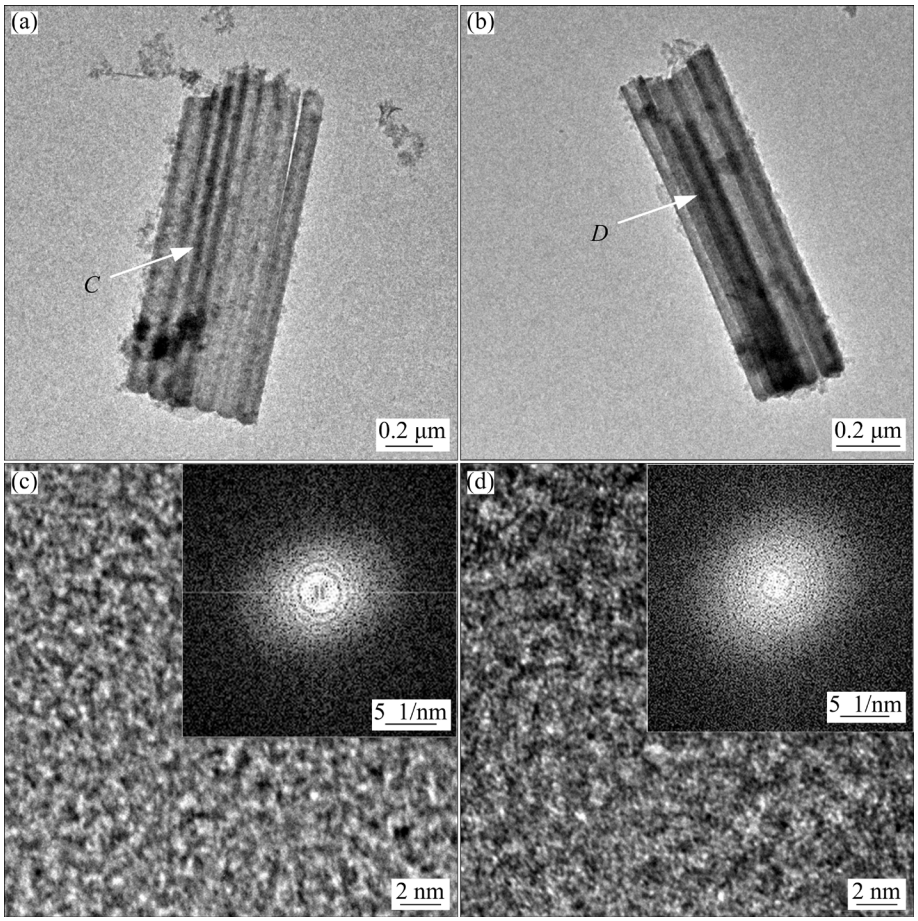

Fig. 8 Bright field TEM image of nanotubes formed on AM-EA (a); Bright field TEM image of nanotubes formed on PM-EA (b); High-resolution TEM image and corresponding FFT pattern of nanotubes formed on AM-EA (c); High-resolution TEM image and corresponding FFT pattern of nanotubes formed on PM-EA (d)

structures grown from Ti-based substrates in fluoride-containing electrolytes are amorphous, since fluoride ions may suppress the crystallization of the oxides [29].

Table 3 presents the compositions of the nanotubes removed from AM-EA and PM-EA samples obtained by the EDS equipped with TEM. The mass fraction ratios of Zr/(Ti+Zr) in the nanotubes on AM-EA and PM-EA are 13.5% and 5.7%, respectively. Such a disparity between the anodized configurations is probably due to the different Zr distributions in the AM and PM substrates. The nanotubes on PM-EA should be mainly formed on Ti-enriched regions, rather than Zr-enriched strips. It is reported that the nanotubes usually contain slightly more Zr than the Ti−Zr-based substrates [30]. However, in this work, after comparing the EDS results as presented in Table 1 and Table 3, it seems that the fractions of Zr in oxide tubes on AM-EA and PM-EA are slightly lower than those in their parent substrate materials (i.e., ~15 wt.% of Zr in AM and ~7.5 wt.% of Zr in PM). Such a contradictory result might result from the relatively low accuracy of EDS.

Table 3 EDS results of points in Figs. 8(a, b) (wt.%)

Point	Ti	Zr	O
C	56.3	8.82	34.88
D	38.44	2.33	59.23

To further evaluate the composition of the nanotubes, AM-EA and PM-EA were investigated by using XPS. Figure 9 shows the spectra of O 1s, Ti 2p, and Zr 3d regions of AM-EA and PM-EA. The solid, dotted, and dot-dash lines show the reported peak positions of binding energy for TiO_2, Zr/Ti oxide (mainly $ZrTiO_4$, named ZT), and ZrO_2, respectively [16]. Besides TiO_2 and ZrO_2, the O 1s spectra of both configurations also show good agreement with the ZT peak at 530.2 eV. The increase of the binding energy of Ti $2p_{3/2}$ in both

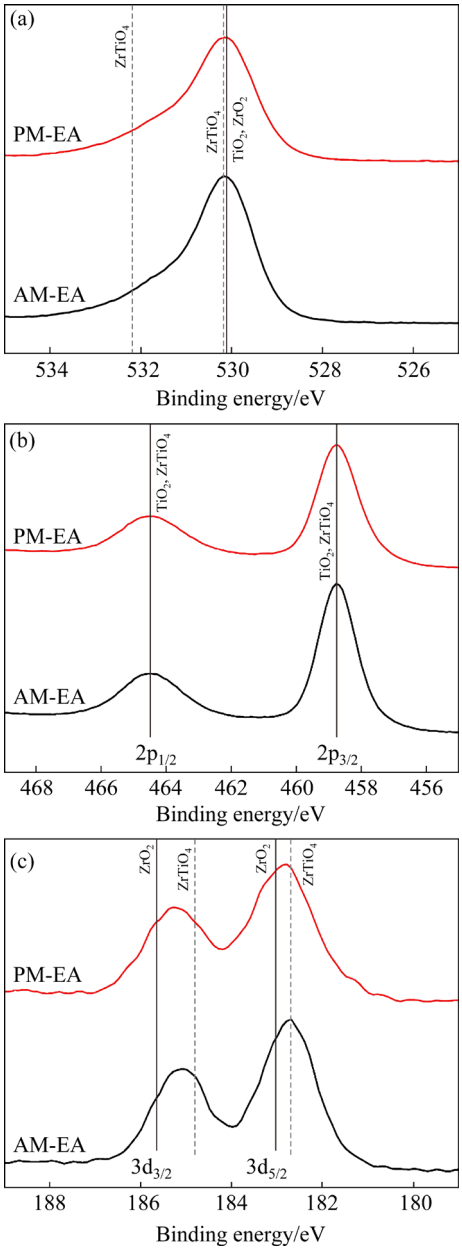

Fig. 9 XPS spectra of AM-EA and PM-EA: (a) O 1s; (b) Ti 2p; (c) Zr 3d

AM-EA and PM-EA (458.8 eV) compared with the binding energy of 458.4 eV in pure TiO_2 [30] obviously reveals that the chemical state of Ti in the nanotubes is very sensitive to the introduction of Zr (even as low as ~5.7 wt.% Zr in the oxide tubes on PM-EA). Besides, the shift of Zr 3d of AM-EA compared with that of PM-EA might be attributed to the different Zr contents in the oxide nanotubes. In a word, based on the TEM, EDS, and XPS results, the nanotubes on both AM-EA and PM-EA consist of the same amorphous phases including ZT with excess TiO_2 and ZrO_2, although the former tubes contain more Zr.

The above-mentioned differences in microstructure between the oxide nanotubes formed on AM-EA and PM-EA should be mainly attributed to the following two aspects: the grain orientation preference and the composition heterogeneity.

The AM sample shows a uniform Zr distribution, and the microstructure is composed of coarse equiaxed grains. The Zr distribution of PM samples is not uniform with Zr-rich strips. Moreover, the PM sample contains finer grains and obviously preferred orientations. The AM-EA sample has a smooth nanotube surface with fewer cracks. The nanotube surface of PM-EA is not smooth and presents directional microcracks. It is not a coincidence to exhibit comparable widths of Zr-enriched strips on PM and microcracks on PM-EA as well as similar oriented structures of the strips and microcracks. Differences in preferred orientations of grains can significantly affect the anodization behavior and thus lead to the formation of different types of nanotube arrays on Ti-based substrates [31]. The (0001) plane of α-phase in Ti-based materials is the close-packed plane, and highly electronically conductive oxide films are usually formed on it. On the (*hki0*) plane, a thicker but less conductive film is grown [32]. The formation of the oriented microcracks on PM-EA is highly dependent on the textures on the parent PM substrate. As illustrated in Fig. 4(a), most (0001)-oriented grains lie in Zr-enriched strips, while the coarse ones in Ti-enriched areas are usually either $(10\bar{1}0)$-oriented or $(2\bar{1}\bar{1}0)$-oriented. Since it is much more difficult to start the electrochemical anodic oxygen evolution on conductive (0001)-oriented grains than on passive (*hki*0)-oriented grains, the elongated pristine Zr-enriched strips become microcracks among the as-formed oxide nanotubes in Ti-enriched regions. Besides, since the growth rate of nanotubes gradually increases with decreasing the planar atomic density of the Ti-based parent material [32], the different heights of the nanotube clusters on PM-EA as presented in Figs. 5(c, d) should be probably due to the various orientations of the grains in Ti-enriched regions in PM as shown in Fig. 4(a).

The chemical composition of Ti-based substrates also plays an important role in determining the morphology of the anodized samples. Although the oxide nanotubes on AM-EA

and PM-EA show similar phase constitutions (see Fig. 8), their significantly different Zr contents (see Table 3) suggest different formation mechanisms. Zr is usually considered a neutral element, but its content can significantly influence the anodization behavior [18]. Thus, the Zr/(Ti+Zr) ratio in the Ti−Zr binary system is of great importance. The uniform distribution of Ti and Zr in the AM Ti−15Zr alloy (see Fig. 3(b)) inevitably leads to a relatively smooth surface of AM-EA, as shown in Figs. 5(a, b), because when the content of Zr is low (e.g., 17.6 wt.%), the surface of the nanotube arrays is smooth, similar to that of pure Ti [30]. In contrast, it is reported that when the Zr content is higher than 20 wt.%, the nanotubes become more separate and tend to bend at the top [29]. Therefore, considering the sharp Zr compositional gradient from Zr-enriched strips (over 20 wt.%) to Ti-enriched regions (less than 10 wt.%) as presented in Fig. 3(d) and Table 1, the nanotubes formed on the boundaries between the adjacent Zr-enriched strip and Ti-enriched region might be bent and around the lateral of nanotube clusters, as shown in Figs. 5(c, d). According to the SEM results, the nanotubes in PM-EA have a trench structure. The formation of such a structure may result from the grain size, grain orientation, and Zr content. If possible, it can be called strip-like distributed nanotube area.

From the topographical point of view, AM-EA and PM-EA are similar at the nano-scale, since the nanotubular diameters on both configurations are almost the same (see Fig. 5). As illustrated before, the diameter of nanotubes grown on Ti-based substrates is highly dependent on various factors, such as anodization voltage and electrolyte, and substrate composition [13,33]. In this study, the same voltage and electrolyte were used for the anodization of AM and PM samples. Moreover, the Zr contents in AM (~15 wt.%) and in Ti-enriched regions (~7.5 wt.%) are below the widely accepted threshold (~20 wt.% [29]) for geometry change. Therefore, it is reasonable to obtain similar nano-scaled geometry on AM-EA and PM-EA. However, the latter material shows more micron-scaled structures than the former, as presented in Figs. 5(c, d). The presence of nanotube clusters and oriented microcracks considerably increases the surface profile deviation and surface area ratio, which probably influences the mechanical properties of the substrates. Elastic modulus is one of the most important parameters when selecting proper implant materials [34]. After anodization, elastic modulus of the implant surface decreases when considering the extremely high area aspect ratio of the nanotubular structures [35]. So, it is reasonable to assume that the formation of microcracks might further decrease the surface stiffness, and even possibly reach the modulus of native bone tissue. As reported in our previous work [23], the PM Ti−15Zr shows significantly higher tensile strength (~915 MPa) and elongation (>20%) than the arc-melted Ti−Zr alloys with similar Zr contents (600−800 MPa and ~15%, respectively) [36−38], so it is reasonable to assume that PM-EA may show better tensile properties than AM-EA samples. It is important to note that the microcracks of nanotubes may lead to stress concentration [39], and thus be probably detrimental to the fatigue behavior.

3.2 Wettability

The initial contact angles of AM, PM, AM-EA, and PM-EA are shown in Fig. 10. The results show that the contact angles of AM and PM are 49.8° and 49.5°, respectively. But after anodization, the contact angles significantly decrease to 3.0° (AM-EA) and 2.1° (PM-EA), showing super-hydrophilicity.

The implants with super-hydrophilicity are sometimes favored clinically because the interaction between the dental implants and the surrounding tissues usually begins from the water displacement [40]. Generally, surface free energy is related to the surface topography [41]. In this case,

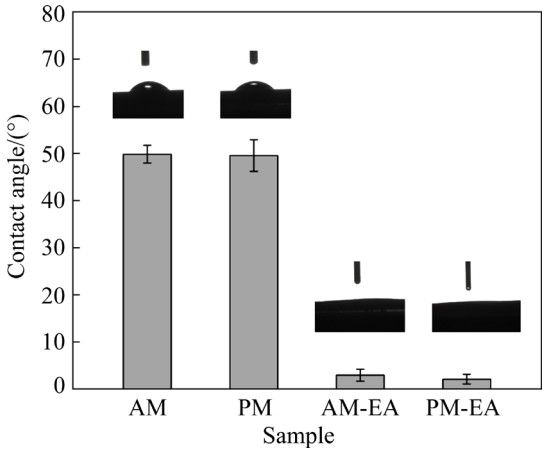

Fig. 10 Initial contact angles and optical images of drops on AM, PM, AM-EA, and PM-EA

the anodized groups show much better wettability compared with the polished ones, suggesting the important role the nanotubular structures play.

3.3 Protein absorption

Figure 11 shows the amount of protein adsorption on AM, AM-EA, PM, and PM-EA. After incubation for 2 h, anodized samples adsorb a significantly higher amount of protein than non-anodized samples. In addition, the protein adsorption on PM-EA is significantly higher than that on AM-EA.

Protein adsorption plays a dominant role in regulating cell attachment. The adsorption of a protein layer is the initial process occurring at the implant−biological ambiance contact [42], so the protein adsorption behavior was evaluated before performing cell assessments in this work. Although the hydrophobic surfaces are widely considered as preferred ones for protein adsorption, the anodized samples with lower contact angles present a higher amount of adsorbed protein than the other two configurations. Such behavior should be attributed to the nano-scale features of AM-EA and PM-EA since the thin walls of the nanotubes might be

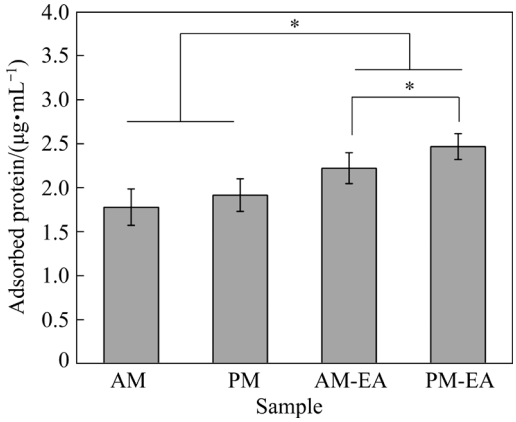

Fig. 11 Protein adsorption level of BSA on four configurations ($* p < 0.05$)

preferential adsorption sites for the protein. PM-EA shows a micro/nano-scaled structure, and the values of R_a, R_q and R_z are significantly higher than those of AM-EA. The larger specific surface area of the former can increase the surface free energy of the material and provide more abundant protein adsorption sites [8].

3.4 Cell adhesion

Figure 12 shows the SEM images of adhered

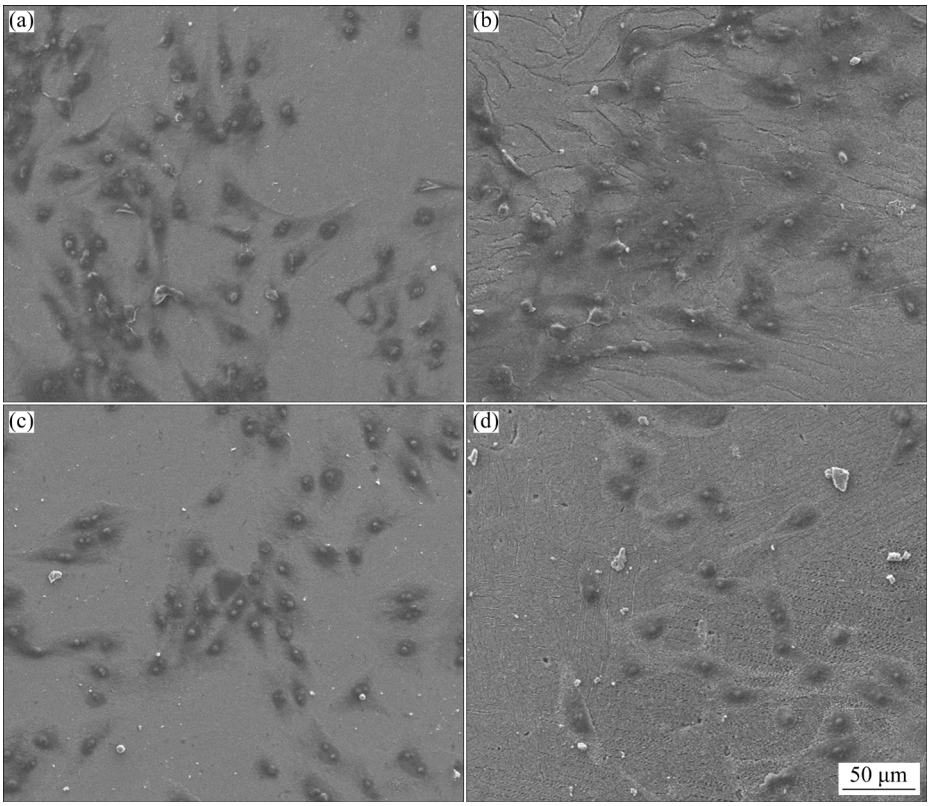

Fig. 12 MG63 cell morphologies on samples in four groups after 24 h of incubation: (a) AM; (b) AM-EA; (c) PM; (d) PM-EA

MG63 cells cultured for 24 h on the four configurations (AM, PM, AM-EA, and PM-EA). Most MG63 cells show a spindle and polygonal shape. Moreover, the polygonal cells exhibit numerous filopodia. Filopodia cause localized adhesion to the matrix, connecting cells to the material surface. This phenomenon indicates that both the anodized surface and original surface are conducive to the formation of polygonal cells and cell adhesion.

3.5 Cell proliferation

The proliferation of MG63 cells on the four configurations is shown in Fig. 13. It is obvious that the cell proliferation on PM-EA cultured for 3 d and 5 d is significantly improved compared with the other three groups. In addition, the OD level of the AM group is significantly lower than that of the other three groups. Although all configurations present good cell adhesion behavior (see Fig. 12), the cell proliferation in PM-EA is significantly higher than that in other groups, as shown in Fig. 13. Such a result indicates that a surface with both nano-scaled and micron-scaled topography may be preferential for long-term implantation. In the cell adhesion experiments performed by KONATU et al [27], the number of cells on surface of Ti−15Zr nanotubes was higher than that of the polished samples. These results agree with other studies for surfaces containing TiO_2 nanotubes [43,44], but no significant difference in initial adhesion was observed in our experiments. However, after several days of cell proliferation, all surfaces of the nanotubes show significantly better cell proliferation.

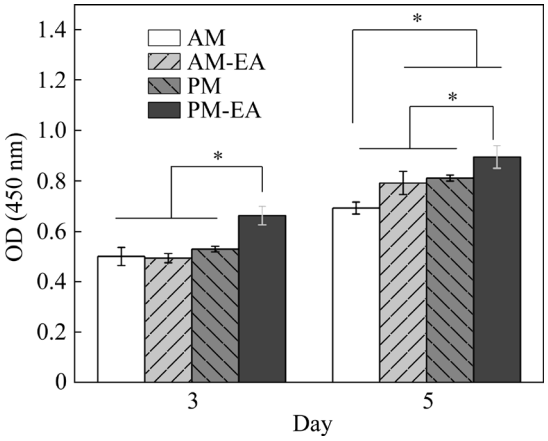

Fig. 13 Proliferation of MG63 cells evaluated by CCK-8 test ($* p < 0.05$)

4 Conclusions

(1) The Ti−15Zr alloy obtained by powder metallurgy and subsequent hot rolling shows Zr segregation, bimodal grain size distribution, and preferred orientations.

(2) The (0001)-oriented fine grains lead to the formation of the microcracks, while the sharp Zr gradient is also responsible for the formed nanotubular clusters.

(3) The anodized Ti−15Zr alloy with both micron-scaled roughness and nano-sized structures shows better hydrophilicity and cell response, suggesting the great potential as a dental implant material.

Acknowledgments

This work was financially supported by the National Natural Science Foundation of China (No. 52171114) and the Innovation-oriented Advanced Technology and Industrial Technology Program Project of Hunan Province, China (No. 2020SK2017).

References

[1] JI Xiao-wei, LIU Pin-ting, TANG Jin-cheng, WAN Chang-jun, YANG Yan, ZHAO Zhi-li, ZHAO Da-peng. Different antibacterial mechanisms of titania nanotube arrays at various growth phases of *E. coli* [J]. Transactions of Nonferrous Metals Society of China, 2021, 31: 3821−3830.

[2] SCHIFF L J, GRAHAM J A. Cytotoxic effect of vanadium and oil-fired fly ash on hamster tracheal epithelium [J]. Environmental Research, 1984, 34: 390−402.

[3] ALTUNA P, LUCAS-TAULÉ E, GARGALLO-ALBIOL J, FIGUERAS-ÁLVAREZ O, HERNÁNDEZ-ALFARO F, NART J. Clinical evidence on titanium-zirconium dental implants: A systematic review and meta-analysis [J]. International Journal of Oral and Maxillofacial Surgery, 2016, 45: 842−850.

[4] HO Wen-fu, CHEN Wei-kai, WU Shin-ching, HSU Hsueh-chuan. Structure, mechanical properties, and grindability of dental Ti−Zr alloys [J]. Journal of Materials Science: Materials in Medicine, 2008, 19: 3179−3186.

[5] CORDEIRO J M, BELINE T, RIBEIROC A L R, RANGEL E C, da CRUZ N C, LANDERS R, FAVERANI L P, VAZ L G, FAIS L M G, VICENTE F B, GRANDINI C R, MATHEW M T, SUKOTJO C, BARAO V A R. Development of binary and ternary titanium alloys for dental implants [J]. Dental Materials, 2017, 33: 1244−1257.

[6] CORDEIRO J M, BARÃO V A R. Is there scientific evidence favoring the substitution of commercially pure titanium with titanium alloys for the manufacture of dental

implants? [J]. Materials Science and Engineering C, 2017, 71: 1201−1215.

[7] ZHAO Da-peng, CHEN Yu-kai, CHANG Ke-ke, EBEL T, LUTHRIGNER-FEYERABEND B J C, WILLUMEIT-RÖMER R, PYCZAK F. Surface topography and cytocompatibility of metal injection molded Ti−22Nb alloy as biomaterial [J]. Transactions of Nonferrous Metals Society of China, 2018, 28: 1342−1350.

[8] ZHAO Da-peng, TANG Jin-cheng, NIE He-min, ZHANG Yuan, CHEN Yu-kai, ZHANG Xu, LI Hui-xing, YAN Ming. Macro-micron-nano-featured surface topography of Ti−6Al−4V alloy for biomedical applications [J]. Rare Metals, 2018, 37: 1055−1063.

[9] BOYAN B D, HUMMERT T W, DEAN D D, SCHWARTZ Z. Role of material surfaces in regulating bone and cartilage cell response [J]. Biomaterials, 1996, 17: 137−146.

[10] KIESWETTER K, SCHWARTZ Z, HUMMERT T, COCHRAN D, SIMPSON J, DEAN D, BOYAN B. Surface roughness modulates the local production of growth factors and cytokines by osteoblast-like MG-63 cells [J]. Journal of Biomedical Materials Research: An Official Journal of the Society for Biomaterials and the Japanese Society for Biomaterials, 1996, 32: 55−63.

[11] RAINES A L, OLIVARES-NAVARRETE R, WIELAND M, COCHRAN D L, SCHWARTZ Z, BOYAN B D. Regulation of angiogenesis during osseointegration by titanium surface microstructure and energy [J]. Biomaterials, 2010, 31: 4909−4917.

[12] GITTENS R A, MCLACHLAN T, OLIVARES-NAVARRETE R, CAI Y, BERNER S, TANNENBAUM R, SCHWARTZ Z, SANDHAGE K H, BOYAN B D. The effects of combined micron-/submicron-scale surface roughness and nanoscale features on cell proliferation and differentiation [J]. Biomaterials, 2011, 32: 3395−3403.

[13] ABBAS W A, ABDULLAH I H, ALI B A, AHMED N, MOHAMED A M, REZK M Y, ISMAIL N, MOHAMED M A, ALLAM N K. Recent advances in the use of TiO_2 nanotube powder in biological, environmental, and energy applications [J]. Nanoscale Advances, 2019, 1: 2801−2816.

[14] BELTRAN-PARTIDA E, VALDEZ-SALAS B, MORENO-ULLOA A, ESCAMILLA A, CURIEL M A, ROSALES-IBANEZ R, VILLARREAL F, BASTIDAS D M, BASTIDAS J M. Improved in vitro angiogenic behavior on anodized titanium dioxide nanotubes [J]. Journal of Nanobiotechnology, 2017, 15: 1−21.

[15] CHERNOZEM R V, SURMENEVA M A, IGNATOV V P, PELTEK O O, GONCHARENKO A A, MUSLIMOV A R, TIMIN A S, TYURIN A I, IVANOV Y F, GRANDINI C R. Comprehensive characterization of titania nanotubes fabricated on Ti−Nb alloys: Surface topography, structure, physicomechanical behavior, and a cell culture assay [J]. ACS Biomaterials Science & Engineering, 2020, 6: 1487−1499.

[16] YASUDA K, SCHMUKI P. Formation of self-organized zirconium titanate nanotube layers by alloy anodization [J]. Advanced Materials, 2007, 19: 1757−1760.

[17] MCHALE A E, ROTH R S. Investigation of the phase transition in $ZrTiO_4$ and $ZrTiO_4$−SnO_2 solid solutions [J]. Journal of the American Ceramic Society, 1983, 66: C-18−C-20.

[18] MAJCHROWICZ A, ROGUSKA A, MAJCHROWICZ K, PISAREK M, HOŁDYŃSKI M, BAZARNIK P, LEWANDOWSKA M. Influence of microstructural features on the growth of nanotubular oxide layers on β-phase Ti−24Nb−4Zr−8Sn and α+β-phase Ti−13Nb−13Zr alloys [J]. Surface and Coatings Technology, 2021, 425: 127695.

[19] MACAK J M, JAROSOVA M J, GER A, SOPHA H, KLEMENTOV M. Influence of the Ti microstructure on anodic self-organized TiO_2 nanotube layers produced in ethylene glycol electrolytes [J]. Applied Surface Science, 2016, 371: 607−612.

[20] SOPHA H, TESAR K, KNOTEK P, J GER A, HROMADKO L, MACAK J M. TiO_2 nanotubes grown on Ti substrates with different microstructure [J]. Materials Research Bulletin, 2018, 103: 197−204.

[21] BERNER S, DARD M, GOTTLOW J, MOLENBERG A, WIELAND M. Titanium-zirconium: A novel material for dental implants [J]. Eur Cells Mater, 2009, 17: 189−205.

[22] QUIRYNEN M, AL-NAWAS B, MEIJER H J A, RAZAVI A, REICHERT T E, SCHIMMEL M, STORELLI S, ROMEO E. Small-diameter titanium G rade IV and titanium−zirconium implants in edentulous mandibles: Three-year results from a double-blind, randomized controlled trial [J]. Clinical Oral Implants Research, 2015, 26: 831−840.

[23] LIU Yong, TANG Han-chun, HUANG Qian-li, ZHAO Da-peng, HE Jun-yang, CAO Yuan-kui, SONG Min, LIU Bin, OUYANG Si-hui. Strong-yet-ductile Ti−Zr alloys through high concentration of oxygen strengthening [J]. Transactions of Nonferrous Metals Society of China, 2020, 30: 2449−2458.

[24] TANG Han-chun, LIU Yong, LIU Chao-qiang, ZHAO Da-peng, SONG Min. Achieving high strength and large ductility via Zr-rich stripes in Ti−15Zr alloy [J]. Materials Letters, 2022, 318: 132194.

[25] DING Chao, SHI Qi, LIU Xin, ZHENG Li, LI Run-xia, HANG Zheng-xiang, YU Bao-yi, WU Wei. Microstructure and mechanical properties of PM Ti600 alloy after hot extrusion and subsequent annealing treatment [J]. Materials Science and Engineering A, 2019, 748: 434−440.

[26] KIM W G, CHOE H C. Nanostructure and corrosion behaviors of nanotube formed Ti−Zr alloy [J]. Transactions of Nonferrous Metals Society of China, 2009, 19: 1005−1008.

[27] KONATU R T, DOMINGUES D D, ESCADA A L A, CHAVES J A M, NETIPANYJ M F D, NAKAZATO R Z, POPAT K C, GRANDINI C R, CLARO A A. Synthesis and characterization of self-organized TiO_2 nanotubes grown on Ti−15Zr alloy surface to enhance cell response [J]. Surfaces and Interfaces, 2021, 26: 101439.

[28] YASUDA K, MACAK J M, BERGER S, GHICOV A, SCHMUKI P. Mechanistic aspects of the self-organization process for oxide nanotube formation on valve metals [J]. Journal of the Electrochemical Society, 2007, 154: C472−C478.

[29] TSUCHIYA H, AKAKI T, NAKATA J, TERADA D, TSUJI N, KOIZUMI Y, MINAMINO Y, SCHMUKI P, FUJIMOTO S. Metallurgical aspects on the formation of self-organized anodic oxide nanotube layers [J]. Electrochimica Acta, 2009,

54: 5155−5162

[30] LIU Gang, LU Hao-feng, CHEN Zhi-gang, LI Feng, WANG Lian-zhou, WATTS JOSH, LU Gao-qing, CHENG Hui-ming. Ti−Zr−O nanotube arrays with controlled morphology, crystal structure and optical properties [J]. Journal of Nanoscience and Nanotechnology, 2009, 9: 6501−6510.

[31] CRAWFORD G A, CHAWLA N. Tailoring TiO_2 nanotube growth during anodic oxidation by crystallographic orientation of Ti [J]. Scripta Materialia, 2009, 60: 874−877.

[32] LEONARDI S, RUSSO V, LI BASSI A, di FONZO F, MURRAY T M, EFSTATHIADIS H, AGNOLI A, KUNZE-LIEHHAEUSER J. TiO_2 nanotubes: Interdependence of substrate grain orientation and growth rate [J]. ACS Applied Materials & Interfaces, 2015, 7: 1662−1668.

[33] ZHANG Lan, HAN Yong. Effect of nanostructured titanium on anodization growth of self-organized TiO_2 nanotubes [J]. Nanotechnology, 2010, 21: 055602.

[34] ZHAO Da-peng, CHANG Ke-ke, EBEL T, QIAN Ma, WILLUMEIT R, YAN M, PYCZAK F. Microstructure and mechanical behavior of metal injection molded Ti−Nb binary alloys as biomedical material [J]. Journal of the Mechanical Behavior of Biomedical Materials, 2013, 28: 171−182.

[35] TANG Hao, LI Ying, MA Jian-wei, ZHANG Xian-lin, LI Bao-e, LIU Shi-min, DAI Fang-fei, ZHANG Xiang-qian. Improvement of biological and mechanical properties of titanium surface by anodic oxidation [J]. Bio-medical Materials and Engineering, 2016, 27: 485−494.

[36] MORENO J M C, POPA M, IVANESCU S, VASILESCU C, DROB S I, NEACSU E I, POPA M V. Microstructure, mechanical properties, and corrosion resistance of Ti−20Zr alloy in undoped and NaF doped artificial saliva [J]. Metals and Materials International, 2014, 20: 177−187.

[37] KONDOH K, FUKUO M, KARIYA S, SHITARA K, LI Shu-feng, ALHAZAA A, UMEDA J. Quantitative strengthening evaluation of powder metallurgy Ti−Zr binary alloys with high strength and ductility [J]. Journal of Alloys and Compounds, 2021, 852: 156954.

[38] ZHOU Yun-kai, JING Ran, MA Ming-zhen, LIU Ri-ping. Tensile strength of Zr−Ti binary alloy [J]. Chinese Physics Letters, 2014, 30: 116201.

[39] CHENG Wen-juan, LIU Yong, ZHAO Da-peng, LIU Bin, TAN Yan-ni, WANG Xiao-gang, TANG Han-chun. Crack propagation behavior of inhomogeneous laminated Ti−Nb metal-metal composite [J]. Transactions of Nonferrous Metals Society of China, 2019, 29: 1882−1888.

[40] BAIER R E. Surface behaviour of biomaterials: The theta surface for biocompatibility [J]. Journal of Materials Science: Materials in Medicine, 2006, 17: 1057−1062.

[41] DRELICH J, CHIBOWSKI E, MENG D D, TERPILOWSKI K. Hydrophilic and superhydrophilic surfaces and materials [J]. Soft Matter, 2011, 7: 9804−9828.

[42] SILVA-BERMUDEZ P, RODIL S E. An overview of protein adsorption on metal oxide coatings for biomedical implants [J]. Surface and Coatings Technology, 2014, 233: 147−158.

[43] KUMERIA T, MON H, AW M S, GULATI K, SANTOS A, GRIESSER H J, LOSIC D. Advanced biopolymer-coated drug-releasing titania nanotubes (TNTs) implants with simultaneously enhanced osteoblast adhesion and antibacterial properties [J]. Colloids and Surfaces B: Biointerfaces, 2015, 130: 255−263.

[44] ESCADA A L, NAKAZATO R Z, CLARO A P R A. Influence of anodization parameters in the TiO_2 nanotubes formation on Ti−7.5Mo alloy surface for biomedical application [J]. Materials Research, 2017, 20: 1282−1290.

非均质显微组织对 Ti−15Zr 合金阳极氧化行为与生物相容性的影响

汤菡纯[1]，赵大鹏[2]，万常俊[2]，李小松[2]，姬晓伟[2]，唐金成[3]，曹远奎[1]，刘 咏[1]

1. 中南大学 粉末冶金国家重点实验室，长沙 410083；
2. 湖南大学 生物学院，长沙 410082；
3. 南方科技大学 材料科学与工程系，深圳 518055

摘 要：研究非均质显微组织对钛合金阳极氧化行为与生物相容性的影响。采用粉末冶金及后续热轧和热处理方法制备非均质 Ti−15Zr 合金，并采用电化学阳极氧化法获得纳米管阵列表面。结果表明，阳极氧化非均质 Ti−15Zr 上形成由纳米管团簇和显微裂纹构成的微纳结构表面，这种结构的形成与条纹状的(0001)取向晶粒以及 Zr 的非均质分布有关。与阳极氧化的电弧熔炼 Ti−15Zr 对照组相比，阳极氧化非均质 Ti−15Zr 具有与其相当的超亲水性，且蛋白吸附与细胞增殖效果更好，这主要是由于后者具有多尺度结构表面。

关键词：Ti−Zr 合金；电化学阳极氧化；成分非均匀性；择优取向；生物相容性

(Edited by Bing YANG)